Nano World Journal

https://doi.org/10.17756/nwj.2018-061

Review Article

Open Access

Perspectives: DOD Inkjets at High and Ultra-Brilliant Light Sources

Rita Graceffa[1], Angelo Accardo[2], Martin Rosenthal[3], Mariia Vlasova[3] and Christian Riekel[3*]

[1]European XFEL, Albert-Einstein-Ring 19, 22761 Hamburg, Germany
[2]LAAS-CNRS, Université de Toulouse, CNRS, F-31400 Toulouse, France
[3]The European Synchrotron, ESRF, CS40220, 38043 Grenoble Cedex 9, France

[*]Correspondence to:
Dr. Christian Riekel
The European Synchrotron
ESRF, CS40220 F-38043
Grenoble Cedex 9, France
Tel: +33 (0)4-76-88-2051
Fax: +33 (0)4-76-88-2542
E-mail: riekel@esrf.fr

Received: December 01, 2018
Accepted: December 31, 2018
Published: January 02, 2019

Citation: Graceffa R, Accardo A, Rosenthal M, Vlasova M, Riekel C. 2018. Perspectives: DOD Inkjets at High and Ultra-Brilliant Light Sources. *NanoWorld J* 4(4): 54-60.

Published by United Scientific Group

Abstract

Droplets generated by inkjets can serve as carriers for biological solutions and objects including nanocrystals. X-ray scattering from ballistic droplets loaded with biological matter provides conformational and structural information in the absence of confining walls of microfluidic systems. Such experiments have been performed stroboscopically on a stream of droplets of sub-nL volume using quasi-continuous synchrotron radiation microbeams in order to obtain sufficient counting statistics. We will discuss methodological and scientific perspectives of X-ray scattering with micro- and nanobeams from individual droplets down to aL volumes based on pulsed ultra-brilliant X-ray free electron laser and 4th generation synchrotron radiation sources.

Keywords

Drop-on-demand inkjets, X-ray scattering, Synchrotron radiation, X-ray free electron laser

Introduction

Liquid sample delivery systems for 3rd generation synchrotron radiation (SR) sources are often based on continuous-flow microfluidics. Indeed, microbeam small-angle X- ray scattering (SAXS) provides access to molecular conformational dynamics with sub-millisecond time resolution [1]. In contrast, serial crystallography based on a stream of aqueous droplets carrying protein nanocrystallites intersecting fs pulses has been pioneered at ultra- brilliant X-ray free electron laser (XFEL) sources [2, 3]. Droplets can also serve as wall-free carriers of solutions -including colloidal- of biological molecules or functional objects like viruses and cells. Temporally uncorrelated droplets limit, however, hit rates from XFEL pulses implying high sample consumption and inefficient use of expensive beam time. Here we are interested in the potential of temporally correlated "ballistic" droplets ejected from drop-on-demand (DOD) inkjets [4, 5] enabling stroboscopic to single droplet scattering depending on the source brilliance. While the examples and discussions will be limited to scattering, droplets are also of interest as carriers for single particle imaging [6]. We will discuss preferentially scattering from ballistic droplets in view of maintaining conformational equilibriums which are important for understanding large functional proteins. Deposition of droplets with biological loads on substrates can, however, be of interest for enhancing molecular concentrations or probing particles at specific locations. Although bearing many similarities to inkjets, acoustic droplet ejection methods [7, 8] will not be discussed.

Droplet ejection and propagation

Thermal DOD inkjets (bubble-jets) used frequently for printing applications allow high-speed, addressable and precise droplet deposition based on multiple print-heads with liquid-filled chambers relied to a common manifold [5, 9, 10]. A heater integrated in each chamber is activated by a µs voltage pulse and the droplet is ejected through an orifice. Experimental science relies, however, generally on single print heads, often based on the piezoelectric compression of a liquid-filled glass capillary due to low fabrications costs [4]. An electronic triggering system allows ejecting a stream of identical, equally spaced droplets of several 10^{th} of µm diameter [4, 10, 11] (Figure 1A-1D).

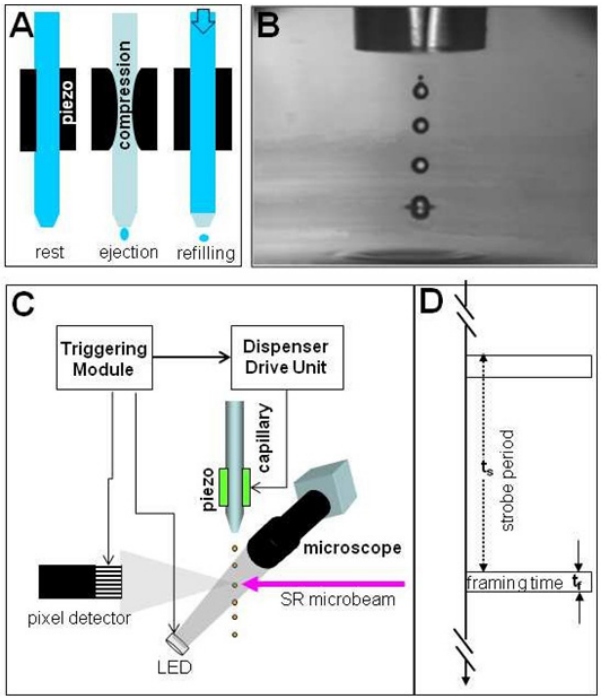

Figure 1: (A) Schematic design of DOD inkjet based on piezoelectric compression of a liquid-filled tube connected to a reservoir (not shown). **(B)** Stroboscopic image of droplets ejected from inkjet nozzle (Courtesy Microdrop Inc.). **(C, D)** Schematic design of stroboscopic setup and triggering sequence used for SR applications (adapted from [12]). During the flight of a droplet through the SR microbeam, the pixel detector frontend is activated by the triggering module during a framing time (t_f). The strobe period (t_s) is triggered by the dispenser driver unit (DDU) acting on the piezo.

This technology is also adapted to ejecting aqueous droplets loaded with fragile biological objects such as living cells [4]. Particularly compact inkjets in planar silicon technology use piezoelectric compression of a liquid-filled reservoir with integrated nozzle [13].

Ballistic droplets ejected from a piezo-driven inkjet propagate in air with speeds (v) up to several 10^{th} m/s and up to about 10 kHz frequency [4, 11]. The dominance of droplet surface energy $\gamma = \sigma 4\pi d^2$ (σ: surface tension, d: diameter) over kinetic energy $E_{kin} = 2/3\rho\pi v^2 d^3$ (v: density, ρ: density) of sub-nL volume droplets results in spherical droplets. Ejection into vacuum is accompanied by an increased evaporation rate and cooling of droplets [14] which can even result in freezing [15].

SR microbeam scattering of ballistic droplets

The high spatial and temporal repeatability of droplets from DOD inkjets enables stroboscopic SR microbeam scattering [16]. Indeed, the stroboscopic optical image of d = 80 µm (268 pL) water droplets ejected at 2 KHz with v = 1.7 m/s is shown in figure 2A. Droplets traversing the 3 µm X-ray focal spot within about 50 µs were probed with t_f = 5 µs in order to avoid blurring of the stroboscopic composite image derived from the sequence of SAXS patterns (Figure 2B) [12, 17]. To obtain sufficient counting statistics ~2 x 10^4 patterns corresponding to ~100 ms overall exposure with ~10^7 photons were accumulated at each mesh-position [12]. X-ray optics and ESRF source improvements allow currently obtaining the same statistics for about 100 patterns per mesh-position [18]. SAXS patterns from aqueous droplets loaded with biological molecules such as cytochrome C (Figure 2C, 2D) [12] or wide-angle X-ray scattering (WAXS) patterns from molten paraffin droplets [19] were obtained in the same way.

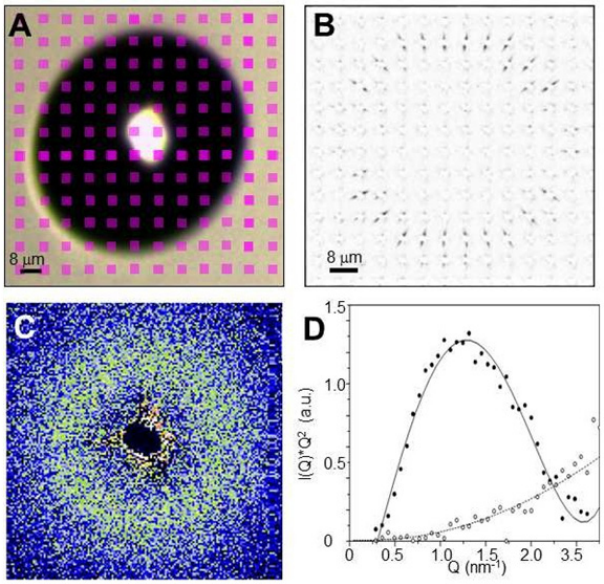

Figure 2: (A) Stroboscopic (t_s = 500 ms) optical image of d = 80 µm water droplet (268 pL) overlaid with a schematic pattern of position and size of the X-ray focal spots during a mesh-scan. **(B)** Stroboscopic composite image of droplet based on a mesh of SAXS patterns obtained at the ESRF-ID13 beamline with a framing time t_f = 5 µs. The interface is revealed by refractive streaks [12]. **(C)** MicroSAXS pattern from 2 mM cytochrome C in acid buffer solution droplet. **(D)** Kratky plot of azimuthally averaged cytochrome C scattering. Solid circles: protein; open circles: HCl buffer scattering [12].

This approach can be extended to the synchronization of two inkjets providing access to droplet coalescence. Indeed, the stroboscopic optical image of droplets ejected from two inkjets is shown in figure 3A [20]. Excess kinetic energy resulting in damped shape oscillations of the merged droplets resemble chaotic advection in plugs with two components moving through winding microfluidics channels, enhancing mixing and providing access to sub-ms reaction kinetics [21].

Figure 3B shows stroboscopic composite images (heat maps) at two times after the contact of pH 2 solution droplets of cytochrome C with pH 4.6 buffer droplets resulting in protein folding [20]. Protein density redistribution is observed at the ms time-scale as the pixels of the composite images correspond to the integral protein scattering. Indeed, the heavier protein molecules appear to be pushed at 2 ms to the rim, presumably involving chaotic advection [21]. At 4 ms the protein is nearly homogeneously redistributed with a central hole remaining. Such experiments are limited, however, at the ESRF -a 3rd generation SR source- by rather long set-up times and the few heat maps obtained thus far do not reaching the time-scale of protein chain condensation. Indeed, two kinetic phases at the sub-ms scale with the smallest at < 160 µs lifetime have been identified by SAXS using continuous flow microfluidic mixing [22].

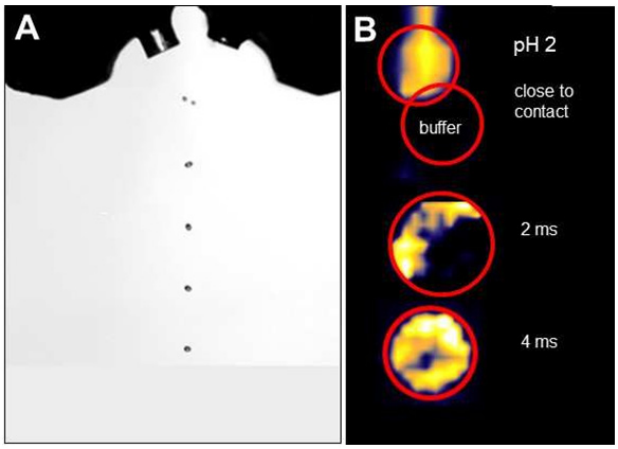

Figure 3: (A) Stroboscopic optical image of droplet ejection from two inkjet heads at an approximate angle of 45° [20]. **(B)** Stroboscopic composite images of the coalescence of pH 2 Cytochrome C and pH 4.6 buffer droplets. The pixels in the images corresponding to the integrated SAXS intensity reveal the protein location. The buffer droplet can be localized by mapping the interface refraction (adapted from [20]). Red contours are guides for the eye and do not show the anisotropy of the merged droplets. The time is defined relative to the contact point.

Perspectives for droplet probing by single pulses at ultra-brilliant light sources

Probing droplets by X-ray pulses (or flashes) from ultra-brilliant light sources allows reducing droplet volumes, sample consumption and provides access to ultra-short time-scales of coalescence processes. We will consider two state-of-the art light sources providing hard X-rays: (i) the linear electron accelerator-based EuXFEL (European XFEL) in Hamburg (Germany) and (ii) the upcoming (2020) electron storage ring-based ESRF/EBS (Extremely Bright Source) in Grenoble (France) [23] as an example for a 4th generation SR source.

The EuXFEL is based on pulse-trains of 2700 pulses of 50 f_s fwhm (full-width-half-maximum) with an inter-pulse separation of 220 ns (Figure 4). The flux for the fully commissioned SPB/SFX (Single Particles, Clusters, and Biomacromolecules & Serial Femtosecond Crystallography) instrument is expected to be 1-8 x 10^{12} photons/pulse in 0.1/1 µm focal spots [24]. ESRF/EBS will provide variable filling patterns for an upper limit of 932 bunches of electrons in the storage ring (Figure 4). Inter-pulse distances and pulse-trains can be changed according to specific filling patterns. The strongest undulator harmonics will provide a flux of ~10^{10} photons/pulse for a $\Delta\lambda/\lambda$~2.8*10^{-2} band-width (pink beam) [25, 26], enabling single pulse scattering with µm to sub- µm spots for the size of droplets shown in figure 2A-2C. Scaling with the volume suggests that droplets of d = 8 µm (268 aL) for EBS/ESRF and d = 1.7 µm (2.5 aL) for EuXFEL should show equivalent scattering with a single pulse as d = 80 µm droplets (268 pL) at the ESRF-ID13 beamline (Figure 2B and 2C).

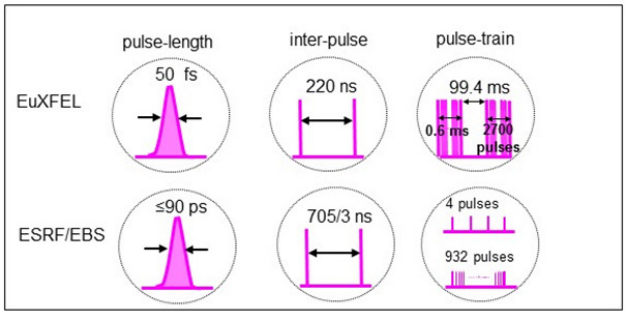

Figure 4: EuXFEL and ESRF/EBS source pulse-length, inter-pulse separations and pulse-trains (EuXFEL pulse-length estimated; ESRF/EBS pulse-length somewhat variable with filling patterns). The ESRF/EBS inter-pulse and pulse- train parameters are shown for homogeneous filling-patterns of 4 and 932 electron bunches for a bunch revolving time of 2.82 µs. Other and more complex filling-patterns are listed in: www.esrf.eu/Accelerators/Operation/Modes.

The interaction of a 70 fs fwhm XFEL pulse focused to 1 µm with a d~40 µm (~33 pL) inkjet droplet at the LCLS XFEL (Stanford) results in liquid explosions producing fragments perturbing the shape and trajectory of neighboring droplets [27]. Indeed, a droplet absorbs during exposure an energy of about $E_X\alpha_X d$ while the energy density (proportional to the internal droplet pressure buildup) is $E_X\alpha_X d/(2\pi d^3/3)$ where E_X is the X-ray pulse energy and α_X the X-ray absorption coefficient [27]. The effects of fragmentation can be reduced by probing smaller droplets and maximizing the ejection speed. The smallest diameters of droplets from print-heads based on piezo-compression of capillaries are around 30 µm (~14 pL). The ejection of smaller droplets is an active R&D topic in view of high-resolution printing applications [28]. We mention as example electrohydrodynamic jet (E-jet) printing with droplet trajectories defined by the electric field due to an applied voltage between conducting nozzle and substrate. Indeed, 3-5 µm (14-65 aL) aqueous droplets ejected at 1 KHz printing speed [29] and 200 nm droplets (4.2 aL) have been demonstrated [30]. Charging can pose problems for fragile proteins and other ejection technologies for reducing droplet volumes will have to be explored [28]. The practical lower droplet size is set by aerodynamic effects perturbing the trajectory (see also below). Reduction of air drag by He-environment or reduced pressure will increase droplet speed and travel range. Limitations of reduced pressure are set by an

increased evaporation rate resulting in droplet cooling.

Droplet ejection can be triggered by the ~10 Hz EuXFEL pulse-trains but not by the ~4.5 MHz pulse-frequency in a pulse-train. The number of droplets from a single inkjet-head interacting with a single pulse-train could be maximized by increasing speed and frequency. Future R&D should, however, aim at MEMS fabrication, integrating multiple ink-jet heads connected to a common manifold, analogue to high-speed printers. This would for example allow distributing droplets along the about 6 mm long Rayleigh length of the 1 µm focal spot of the SFB/SFX instrument [24], minimizing perturbations by liquid explosions. The effect of liquid explosions will be far less for a pink beam at ESRF/EBS and the flexibility of ESRF/EBS filling patters allows triggering droplet ejection to individual pulses. The impact of radiation damage by factor 10^3 longer pulse-length is difficult assessing as photoelectron escape probability will increase with decreasing droplet size [31].

The correlated sequence and trajectory of pL ballistic droplets allows anticipating novel sample environments. We will use as example a nanocalorimetry chip with a thin Si_3N_4 membrane (Figure 5) allowing modulating the temperature of a sample on the active area for heating rates up to about 2 x 10^4 K/s [33]. This could be used for rapid heating of a droplet with a biological load deposited on the active area. One could also adapt the geometry of the active area for continuously heating of droplets propagating along a trajectory close to the membrane surface by the ascending hot air (Figure 5) providing access to variations of molecular conformational equilibriums in successive droplets. The open geometry is attractive as it permits coupling other fields (electric/magnetic) or laser flashes to biological loads.

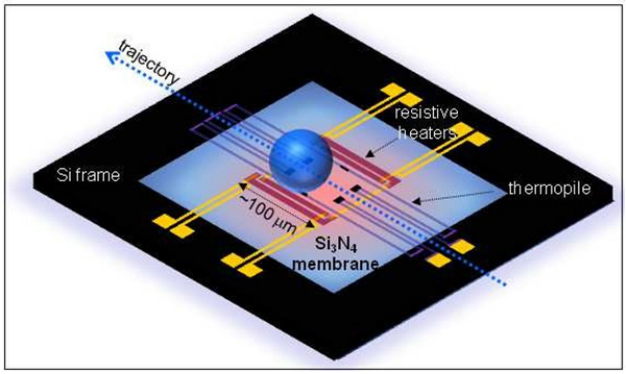

Figure 5: Nanocalorimetry chip based on Si_3N_4 membrane with sputtered resistance heaters and thermopiles on a Si-frame (adapted from [32]). A ballistic droplet evolving close to the membrane is continuously heated along its trajectory across the about 100 x 100 µm² heated zone. Local X-ray scattering provides structural information for a specific temperature which can be modulated by the temperature of the chip.

Probing the onset of coalescence in ultra-small, wall-free volumes is of considerable interest for practical and fundamental studies on topics such as thin film coatings, non-equilibrium thermodynamics of small-scale systems [34, 35] or transformations of biochemical molecules in the presence of local chemical and shearing gradients [36]. Indeed, microscopic models could be developed based on SAXS providing access to molecular shapes and aggregations. Although fluidic simulations on ballistic droplet coalescence have been reported [37, 38], microscopic details on early stages remain largely unknown.

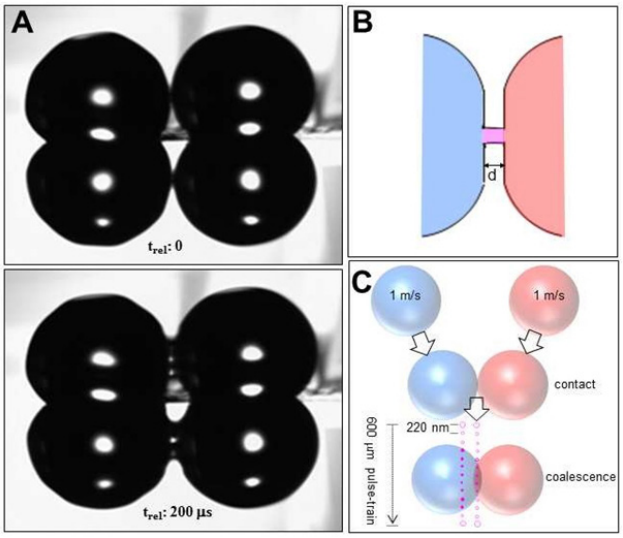

Figure 6: (A) Optical images of the head-on coalescence of two, 1 mm diameter (0.5 µL) water droplets on a planar EWOD device observed by a camera with 200 µs frames just before (t_{rel} = 0) and after (t_{rel} = 200 µs) liquid bridge formation (adapted from [39]). The reflecting silicon surface mirrors the droplets. **(B)** Model of liquid bridge formed during onset of coalescence of hemispherical drops (d = 200 ± 100 nm) [40]. **(C)** Schematic view along the beam direction of the collision of two droplets with d = 40 µm (33.5 pL) moving with v = 1 m/s at an angle of about 45°. The internal frame shows the droplets at rest for three flight times through the focal spot: (i) separated (ii) contact (iii) coalescence (not to scale). The projections of the pulses are depicted as circles for part of the 2700 pulses of a pulse-train. Full circles correspond to pulses hitting the liquid, open circles are outside the liquid. A 2nd pulse- train is shown to the left.

More detailed studies have been performed for head-on-collision processes providing an indication on the time-scale of coalescence onset. Indeed, simulations of low viscosity droplets coalescence reveal the initial formation of a liquid bridge involving an anisotropic flow field [41]. Experimental studies were performed for µL-volume droplets with low interface speeds corresponding to Weber numbers (We) ≤ 1.1 (We = $\rho v^2 d/\sigma$) [42] indicating high contact-line stability [43] while the coalescence of ballistic droplets (e.g. We~3.2 for the droplets in figure 6B [20]) involves deformations. Indeed, optical imaging of water droplets head-on coalescence on a planar superhydrophobic, electrowetting-on-dielectrics (EWOD) device by a fast framing video camera shows the formation of the liquid bridge with t_f = 200 µs framing time [39] (Figure 6A). X-ray phase-contrast imaging with t_f = 472 ns shows the formation of the bridge already at about 5 µs [44] while electrical data place the onset of coalescence at the sub-µs scale [40] (Figure 6B). X-ray scattering of reactive head-on coalescence of $CaCl_2$ and Na_2CO_3 solution droplets at the 100 ms time-scale reveals an amorphous $CaCO_3$ phase preceding the crystalline phases [39]. Here one would

like acceding to sub-µs time scales for observing the first aggregation steps in-situ. This holds also for conformational states at the onset of enzyme/substrate reactions [36]. One can estimate the lowest accessible time-scale (t) for a freshly created interface of diameter d between two droplets for a diffusion process from: $t = d^2*D^{-1}$. For d = 100 nm and a water self-diffusion coefficient of D~10^{-5} $cm^{-2}s^{-1}$ one obtains t~10 ns. This time-scale corresponds to the onset of protein folding accessible to molecular dynamics (MD) simulations, laser-induced temperature jump and dynamic NMR [1].

The practically attainable time-scale depends, however, on the stability of the inkjet setup, droplets trajectory as well as focal spot position and size. X-ray focusing optics at the ESRF has reached the 10 nm scale [45] and the 100 nm focal spot of the EuXFEL SPB/SFX instrument is expected having a drift of less than the beam width [24]. We identify, however several inkjet-related issues to be addressed for reaching stability at sub-µm scale. Indeed, piezo-driven inkjets maintain the droplet trajectory at least to a few microns constant (Figure 2B) but the lower limit is unknown. Compact inkjet-heads in silicon technology with pre-oriented nozzles and a common liquid-filled manifold should be more stable than a mechanical assembly of two inkjets. Active trajectory correction could become necessary for reducing perturbations by air movements or from particles aggregating at the exit of the print-head. This could be based on a superhydrophobic surface [46] where the quasi-contact-free condition between the droplet and the material would result in droplet reflection towards precise trajectories (Figure 7, Supporting Information: Video) by tip-tilt control using piezo-actuators, analogue to astronomical mirrors [47]. The EuXFEL pulse-train in combination with the ultrafast-framing AGIPD detector [24, 48] allows probing the coalescence area of a pair of droplets at a specific coalescence time after their contact without moving the inkjet-heads. Indeed, a pair of 40 µm (33.5 pL) droplets flying with v = 1 m/s through a 100 nm focal spot would be mapped by a single pulse-train with a spatial resolution of 220 nm along a 600 µm trajectory (Figure 6C). Probing droplets at different coalescence times will require, however, changing the nozzle-to-focal spot distance. By displacing the inkjet-head laterally one could map a larger area depending on the stability of the droplets in the beam.

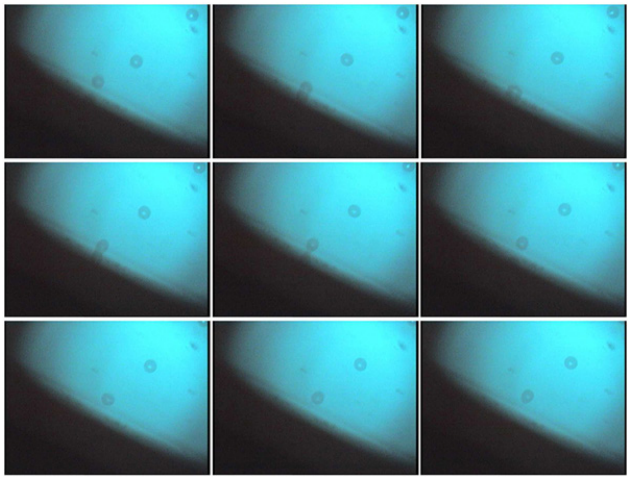

Figure 7: Bouncing of 80 µm diameter (268 pL) aqueous droplets at a frequency of 1 KHz on a silicon superhydrophobic surface.

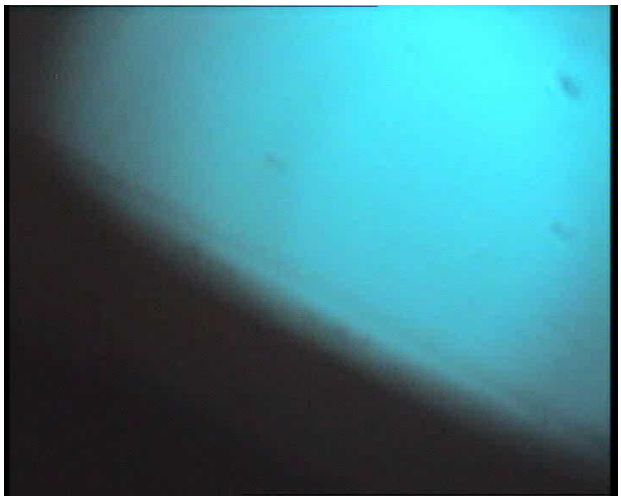

Video: Supporting Information for figure 7

We refrain from a more detailed discussion of the advantages of XFEL versus 4th generation SR sources but we note that the higher XFEL flux/pulse values should allow probing molecular transformations at very early stages of droplets coalescence or serial crystallography with very small droplets. The lower energy deposited for an ESRF/EBS pulse will enable, however, extended mesh- scans in particular at later stages of coalescence. For both types of sources, replacing stroboscopic by single droplet probing will considerable reduce sample volumes and experimental beamtime, enhancing also the stability of the setup.

Conclusions

The use of DOD inkjets at advanced light sources is a largely unexplored area at 3rd generation SR sources but could be particularly interesting for probing droplets loaded with particles or solutions with single pulses at ultra-brilliant light sources. pL to sub-pL liquid sample volumes coupled to fast heating or jumps in chemical potential will enable probing conformational equilibriums or reactive processes down to sub-µs time-scales. We note the wide spread use of CCDs and more recently pixel detectors at SR and XFEL sources, enabled by technology developed for the digital photography mass market. The upcoming of MEMS- based inkjets in high speed graphics and printing applications including 3D bioprinting could facilitate the development of inkjets for scattering applications at ultra-brilliant light sources.

References

1. Graceffa R, Nobrega RP, Barrea RA, Kathuria SV, Chakravarthy S, et al. 2013. Sub-millisecond time-resolved SAXS using a continuous-flow mixer and X-ray microbeam. *J Synchrotron Radiat* 20(Pt 6): 820-825. https://doi.org/10.1107/S0909049513021833

2. Chapman HN, Fromme P, Barty A, White TA, Kirian RA, et al. 2011. Femtosecond X-ray protein nanocrystallography. *Nature* 470(7332): 73-77. https://doi.org/10.1038/nature09750

3. Schlichting I. 2015. Serial femtosecond crystallography: the first five years. *IUCrJ* 2(Pt 2): 246-255. https://doi.org/10.1107/S205225251402702X
4. Lee ER. 2003. Microdrop Generation, CRC Press, FL, USA.
5. Hoath SD. 2016. Fundamentals of Inkjet Printing. Wiley-VCH Verlag GmbH&Co, Weinheim, Germany.
6. Aquila A, Barty A, Bostedt C, Boutet S, Carini G, et al. 2015. The linac coherent light source single particle imaging road map. *Struct Dyn* 2(4): 041701. https://doi.org/10.1063/1.4918726
7. Roessler CG, Kuczewski A, Stearns R, Ellson R, Olechno J, et al. 2013. Acoustic methods for high-throughput protein crystal mounting at next-generation macromolecular crystallographic beamlines. *J Synchrotron Radiat* 20(Pt 5): 805-808. https://doi.org/10.1107/S0909049513020372
8. Fuller FD, Gul S, Chatterjee R, Burgie ES, Young ID, et al. 2017. Drop-on-demand sample delivery for studying biocatalysts in action at X-ray free-electron lasers. *Nat Methods* 14(4): 443-449. https://doi.org/10.1038/nmeth.4195
9. Derby B. 2010. Inkjet printing of functional and structural materials: fluid property requirements, feature stability, and resolution. *Annu Rev Mater Res* 40: 395-414. https://doi.org/10.1146/annurev-matsci-070909-104502
10. Morita N, Khalate A, van Buul AM, Wijshoff H. 2016. Inkjet Printheads. In: Hoath SD (ed) Fundamentals of Inkjet Printing. Wiley-VCH Verlag GmbH&Co, Weinheim, Germany, pp 57-92.
11. Wijshoff H. 2010. The dynamics of the piezo inkjet printhead operation. *Phys Rep* 491(4-5): 77-177.
12. Graceffa R, Burghammer M, Davies R, Ponchut C, Riekel C. 2009. Studying macromolecular solutions without wall effects by stroboscopic small-angle X-ray scattering. *Appl Phys Lett* 94: 062902. https://doi.org/10.1063/1.3078821
13. Laurell T, Wallman L, Nilsson J. 1999. Design and development of a silicon microfabricated flow-through dispenser for on-line picolitre sample handling. *J Micromech Microeng* 9: 369-376. https://doi.org/10.1088/0960-1317/9/4/314
14. Smith JD, Cappa CD, Drisdell WS, Cohen RC, Saykally RJ. 2006. Raman thermometry measurements of free evaporation from liquid water droplets. *J Am Chem Soc* 128(39): 12892-12898. https://doi.org/10.1021/ja063579v
15. Sellberg JA, Huang C, McQueen TA, Loh ND, Laksmono H, et al. 2014. Ultrafast X-ray probing of water structure below the homogeneous ice nucleation temperature. *Nature* 510(7505): 381-384. https://doi.org/10.1038/nature13266
16. Graceffa R. 2010. Development of a drop-on-demand inkjet system for stroboscopic small- and wide-angle X-ray scattering experiments (Doctoral dissertation), Université Joseph-Fourier, Grenoble, France.
17. Riekel C, Burghammer M, Davies R, Gebhardt R, Popov D. 2009. Fundaments of soft condensed matter scattering and diffraction with microfocus techniques. In: Ezquerra TA, Garcia-Gutierrez MC, Nogales A, Gomez M (eds) Applications of synchrotron light to scattering and diffraction in materials, Vol. 776. Springer-Verlag, Berlin, Heidelberg, Germany, pp 91-104.
18. Burghammer M. 2018. Estimation based on monochromatic microbeam flux measured at the ESRF-ID13 beamline. ESRF, Grenoble, France.
19. Graceffa R, Burghammer M, Davies RJ, Riekel C. 2008. Synchrotron radiation microdiffraction of ballistic molten wax microdrops. *Rev Sci Instrum* 79(8): 086106-086101. https://doi.org/10.1063/1.2964108
20. Graceffa R, Burghammer M, Davies R, Ponchut C, Riekel C. 2012. Probing ballistic microdrop coalescence by stroboscopic small-angle X-ray scattering. *Appl Phys Let* 101: 254101. https://doi.org/10.1063/1.4772631
21. Bringer MR, Gerdts CJ, Song H, Tice JD, Ismagilov RF. 2004. Microfluidic systems for chemical kinetics that rely on chaotic mixing in droplets. *Philos Trans A Math Phys Eng Sci* 362(1818): 1087-1104. https://doi.org/10.1098/rsta.2003.1364
22. Akiyama S, Takahashi S, Kimura T, Ishimori K, Morishima I, et al. 2002. Conformational landscape of cytochrome c folding studied by microsecond-resolved small-angle x-ray scattering. *Proc Natl Acad Sci U S A* 99(3): 1329-1334. https://doi.org/10.1073/pnas.012458999
23. ESRF upgrade programme phase II (2015-2019) white paper. ESRF, Grenoble, France.
24. Mancuso AP, Aquila A, Borchers G, Giewekemeyer K, Reimers N. 2013. Technical design report: scientific instrument, single particles, clusters, and biomolecules (SPB). European X-Ray Free-Electron Laser Facility GmbH, Hamburg, Germany.
25. Wulff M. 2018. Estimated flux from undulator harmonics (pink beam) after EBS/ESRF upgrade. ESRF, Grenoble, France.
26. Riekel C. 2015. Protein micro-crystallography: nanotechnology challenges ahead. *NanoWorld J* 1(3): 73-78. http://doi.org/10.17756/nwj.2015-009
27. Stan CA, Milathianaki D, Laksmono H, Sierra RG, McQueen TA, et al. 2016. Liquid explosions induced by X-ray laser pulses. *Nat Phys* 12: 966-971. https://doi.org/10.1038/nphys3779
28. Martin GD, Willis M. 2016. Inkjet technology: what next? In: Hoath SD (ed) Fundamentals of inkjet printing. Wiley-VCH Verlag GmbH&Co, Weinheim, Germany, pp 419-444.
29. Mishra S, Barton KL, Alleyne AG, Ferreira PM, Rogers JA. 2010. High-speed and drop-on-demand printing with a pulsed electrohydrodynamic jet. *J Micromech Microeng* 20: 095026. https://doi.org/10.1088/0960-1317/20/9/095026
30. Park JU, Hardy M, Kang SJ, Barton K, Adair K, et al. 2007. High-resolution electrohydrodynamic jet printing. *Nat Mat* 6: 782-789. https://doi.org/10.1038/nmat1974
31. Nave C, Hill MA. 2005. Will reduced radiation damage occur with very small crystals? *J Synchrotron Radiat* 12(Pt 3): 299-303. https://doi.org/10.1107/S0909049505003274
32. Riekel C, Burghammer M, Snigirev I, Rosenthal M. 2018. Microstructural metrology of tobacco mosaic virus nanorods during radial compression and heating. *Soft Matter* 14: 194-204. https://doi.org/10.1039/C7SM01332A
33. Rosenthal M, Doblas D, Hernandez JJ, Odarchenko YI, Burghammer M, et al. 2014. High-resolution thermal imaging with a combination of nano-focus X-ray diffraction and ultra-fast chip calorimetry. *J Synchrotron Radiat* 21(Pt 1): 223-228. https://doi.org/10.1107/S1600577513024892
34. Reguera D, Rubí JM, Vilar JM. 2005. The mesoscopic dynamics of thermodynamic systems. *J Phys Chem B* 109(46): 21502-21515. https://doi.org/10.1021/jp052904i
35. Miguel RJ. 2007. Non-equilibrium thermodynamics of small-scale systems. *Energy* 32(4): 297-300. https://doi.org/10.1016/j.energy.2005.11.013
36. Schmidt M. 2013. Mix and inject: reaction initiation by diffusion for time-resolved macromolecular crystallography. *Adv Cond Matt Phys* 2013: 167276. https://doi.org/10.1155/2013/167276
37. Trizac E, Hansen JP. 1995. Dynamic scaling behavior of ballistic coalescence. *Phys Rev Lett* 74(21): 4114-4117. https://doi.org/10.1103/PhysRevLett.74.4114
38. van der Bos A, van der Meulen MJ, Driessen T, van den Berg M, Reinten H, et al. 2014. Velocity profile inside piezoacoustic inkjet droplets in flight: comparison between experiment and numerical simulation. *Phys Rev Appl* 1: 014004. https://doi.org/10.1103/PhysRevApplied.1.014004
39. Accardo A, Mecarini F, Leoncini M, Brandi F, Di Cola E, et al. 2013. Fast, active droplet interaction: coalescence and reactive mixing controlled by electrowetting on a superhydrophobic surface. *Lab Chip* 13(3): 332-335. https://doi.org/10.1039/c2lc41193h

40. Case SC, Nagel SR. 2008. Coalescence in low-viscosity liquids. *Phys Rev Lett* 100(8): 084503. https://doi.org/10.1103/PhysRevLett.100.084503

41. Eggers J, Lister JR, Stone HA. 1999. Coalescence of liquid drops. *J Fluid Mech* 401: 293-310. https://doi.org/10.1017/S002211209900662X

42. Brazier-Smith PR, Jennings SG, Latham J, Mason BJ. 1972. The interaction of falling water drops: coalescence. *Proc R Soc Lond A* 326(1566): 393-408. https://doi.org/10.1098/rspa.1972.0016

43. Duan RQ, Koshizuka S, Oka Y. 2003. Two-dimensional simulation of drop deformation and breakup at around the critical weber number. *Nucl Eng Des* 225(1): 37-48 225. https://doi.org/10.1016/S0029-5493(03)00137-7

44. Fezzaa K, Wang Y. 2008. Ultrafast x-ray phase-contrast imaging of the initial coalescence phase of two water droplets. *Phys Rev Lett* 100(10): 104501. https://doi.org/10.1103/PhysRevLett.100.104501

45. da Silva JC, Pacureanu A, Yang Y, Bohic S, Morawe C. et al. 2017. Efficient concentration of high-energy x-rays for diffraction-limited imaging resolution. *Optica* 4(5): 492-495. https://doi.org/10.1364/OPTICA.4.000492

46. Accardo A, Di Fabrizio E, Limongia T, Marinaro G. Riekel C. 2014. Probing droplets on superhydrophobic surfaces by synchrotron radiation scattering techniques. *J Synchrotron Radiat* 21(Pt 4): 643-653. https://doi.org/10.1107/S1600577514009849

47. Watson J. 1997. Tip tilt correction for astronomical telescopes using adaptive control. WESCON/97 *Conference Proceedings*. https://doi.org/10.1109/WESCON.1997.632376

48. Henrich B, Becker J, Dinapoli R, Goettlicher P, Graafsma H, et al. 2011. The adaptive gain integrating pixel detector AGIPD a detector for the European XFEL. *Nucl Instrum Methods Phys Res A* 633(Suppl 1): S11-S14. https://doi.org/10.1016/j.nima.2010.06.107